LANGMUIR

pubs.acs.org/Langmuir Article

MOF@COF Heterostructure Hybrid for Dual-Mode Photoelectrochemical–Electrochemical HIV-1 DNA Sensing

Miaoran Xu, Kun Chen, Lei Zhu, Shuai Zhang, Minghua Wang, Linghao He, Zhihong Zhang,* and Miao Du*

Cite This: *Langmuir* 2021, 37, 13479–13492 Read Online

ACCESS | Metrics & More | Article Recommendations | Supporting Information

ABSTRACT: We developed a novel metal–organic framework (MOF)@covalent–organic framework (COF) hybrid with a hierarchical nanostructure and excellent photoactivity, which further acted as the bifunctional platform of a dual-mode photoelectrochemical (PEC) and electrochemical (EC) biosensor for detecting HIV-1 DNA via immobilizing the HIV-1 DNA probe. First, the presynthesized Cu-MOF nanoellipsoids were used as the template for the in situ growth of the COF network, which was synthesized using copper-phthalocyanine tetra-amine (CoPc-TA) and 2,9-bis[*p*-(formyl)phenyl]-1,10-phenanthroline as building blocks through the Schiff base condensation. In view of the large specific surface area, abundant reserved amino group, excellent electrochemical activity, and high photoactivity, the obtained Cu-MOF@CuPc-TA-COF heterostructure not only can serve as the sensitive platform for anchoring the HIV-1 DNA probe strands but also can be utilized as the signal transducers for PEC and EC biosensors. Thereby, the constructed biosensor shows the sensitive and selective analysis ability toward the HIV-1 target DNA via the complementary hybridization between probe and target DNA strands. The dual-mode PEC and EC measurements revealed that the Cu-MOF@CuPc-TA-COF-based biosensor displayed a wide linear detection range from 1 fM to 1 nM and an extremely low limit of detection (LOD) of 0.07 and 0.18 fM, respectively. In addition, the dual-mode PEC–EC biosensor also demonstrated remarkable selectivity, high stability, good reproducibility, and preferable regeneration ability, as well as acceptable applicability, for which the detected HIV-1 DNA in human serum showed good consistency with real concentrations. Thereby, the present work can open a new dual-mode PEC–EC platform for detecting HIV-1 DNA based on the porous–organic framework heterostructure.

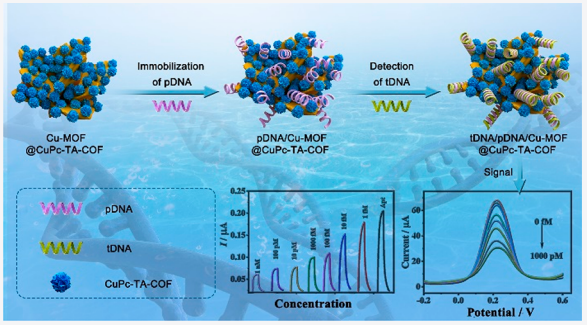

Downloaded via CENTRAL SOUTH UNIV on November 6, 2022 at 02:04:18 (UTC).
See https://pubs.acs.org/sharingguidelines for options on how to legitimately share published articles.

1. INTRODUCTION

As a serious infectious disease, acquired immune deficiency syndrome (AIDS) is caused by HIV-1, leading to a main threat to people's health.[1] HIV damages the immune system over time by destroying the body's ability to fight infections and diseases. Thereby, the early accurate determination of HIV-1 is essential for individual diagnosis, thus saving lives and hampering virus transmission. To date, there have been diverse analysis methods such as electrochemistry,[2] dynamic light scattering,[3] fluorescence,[4] electrochemiluminescence,[5] and photoelectrochemistry (PEC) based on the sensitive sensing of the HIV-1 antibody and/or HIV-1 antigen and HIV-1 DNA. Compared with the immunosensors, different HIV-1 biosensors manufactured for detecting HIV-1 DNA demonstrate the advantages of a low cost and fast response. However, these proposed biosensors often need expensive instruments, laser light, optical imaging, and labeled probes.[6] Consequently, a novel sensing strategy with a convenient device, rapid response, and low cost needs to be explored for sensitive and selective analysis for HIV-1.

Among these techniques, PEC, which is based on the variation of the photoelectric response of different layers coated onto the electrode under photoirradiation,[7,8] has been utilized as a promising analytical method for analyzing diverse targets owing to its intrinsic merits of feasible instrumentation, cheap price, fast analysis, and high selectivity and sensitivity.[9] Beta-cyclodextrin (*β*-CD)-functionalized CdS nanorods (*β*-CD@CdS NRs) were employed as the platform for developing a PEC biosensor for efficiently detecting HIV-1 DNA by combining catalytic hairpin assembly mediated biocatalytic precipitation and the host–guest interaction between adamantine and *β*-CD.[10] CdTe quantum-dot-sensitized ZnO nanorods were used as the cascaded photoactive interface to improve the photoactivity, facilitating the PEC sensing ability

Received: August 24, 2021
Revised: October 15, 2021
Published: November 4, 2021

© 2021 American Chemical Society

https://doi.org/10.1021/acs.langmuir.1c02253
Langmuir 2021, 37, 13479–13492

for detecting HIV-1.[11] Nonetheless, these two present PEC biosensors for the detection of HIV-1 were obtained via a fussy preparation method or the signal amplification technique. Moreover, to construct one efficient PEC biosensor, the photoactive material often plays crucial role for constructing advanced PEC devices and in improving the detection sensitivity.[12] Currently, different nanomaterials such as CdTe, ZnO, TiO_2, g-C_3N_4, and Bi_2S_3[13] serve as the electrode materials for PEC biosensors. Unfortunately, most reported photoactive nanomaterials often suffer from inferior light conversion efficiency, photocorrosion, and unsatisfactory biocompatibility,[14] further limiting their extensive applications.[15] Apart from PEC biosensors, electrochemical (EC) ones have also been explored for sensitively detecting HIV-1[16,17] in light of their features such as high sensitivity, simple detection instrument and data analysis, and small dosage of samples.[18] Consequently, by integrating the advantages of PEC and EC techniques, the dual-mode PEC−EC detection approach is expected to be a promising method for efficiently analyzing targets, such as H_2S,[19] bovine hemoglobin,[20] cytokeratin 19 fragment 21-1,[21] and miRNA-141.[22] Since advanced nanomaterials with high photoactivity and outstanding electrochemical conductivity are fairly scarce, the advancement for the dual-mode PEC−EC sensing technique is greatly hampered. To date, there is no report on the construction of the dual-mode PEC−EC biosensor for the detection of HIV-1. It is expectable to develop a convenient, rapid, and sensitive method based on the dual-mode PEC−EC approach for the early diagnosis of HIV-1 infection.

Most recently, metal−organic frameworks (MOFs) and covalent−organic frameworks (COFs) have aroused incremental attention due to their well-defined topologies, large surface area, and inherent porosities and have displayed vast applications in diverse fields such as catalysis, gas adsorption/separation, biomedicine and biosensing, and molecular separation.[23] By coordinating metal ions and organic linkers, varieties of MOFs have been prepared and acted as the bioplatforms for constructing PEC[24] and EC biosensors[25] thanks to their excellent biocompatibility, strong bioaffinity toward probes, and adjustable structures, along with a possibly outstanding photoactivity or electrochemical activity.[26] Analogously, COFs synthesized using two kinds of organic building blocks via reversible covalent bonds[27] have illustrated broad applications in biosensing fields in light of their virtues including large specific surface area, large pore size, rich functionality, and good PEC activities.[28] Particularly, the optical and electronic performances of MOFs and COFs can be feasibly modulated by selecting metal ions/clusters and organic linkers/building blocks.[29] The abundant porosities endow MOFs or COFs with excellent analyte screening and enrichment, boosting the sensitivity and selectivity of the biosensors.[30,31] Thereby, different MOFs and COFs have been exploited as sensitive platforms for developing biosensors to determine diverse targets such as heavy metal ions, antibiotics, proteins, cancer markers, or bacteria.[32] Thanks to the semiconducting performances that some MOFs exhibit, they have great potential abilities for charge-carrier transport systems in PEC sensing strategies.[33,34] However, only few pristine MOFs have been explored for constructing PEC biosensors.[35] Thereby, diverse nanomaterials such as ZnO, CuO, $ZnIn_2S_4$, CdS, Au-NPs, etc.[36] are often integrated with MOFs to improve the photoactivity and electrochemical activity to afford MOFs PEC sensing performances. Apparently, the pores or channels contained in MOFs can be blocked by these nanomaterials, thus reducing the specific surface area. Due to limited active sites of these MOF-based nanocomposites for anchoring probes (antibodies, DNA, or aptamers), the insufficient limit of detection (LOD) pg mL^{-1} level for 17β-estradiol[37] and squamous cell carcinoma antigen[38] or μg mL^{-1} level for α-casein[35] of the constructed PEC biosensors somehow declines their fascination and vast exploration for practical applications. Moreover, to enhance the detection sensitivities and to improve the photoactivity of MOF-based PEC biosensor platforms, annealing MOFs into transitional metal compounds under high temperature has been applied to solve this issue.[8,39,40] The calcination operation toward MOFs apparently remarkably increases the energy consumption and destructs the features of pristine MOFs, usually leading to the collapse of the intrinsic frameworks of MOFs. It is promising to design and explore the novel heterostructures or nanohybrids based on MOFs, which not only can inherit the advantages of their MOF parents but also display the excellent PEC performance.

In addition, the electron−hole recombination time can be prolonged in some photoactive COFs. For example, porphyrin-COFs (p-COFs) show the enhanced photoelectric conversion efficiency under light irradiation.[41] Consequently, p-COFs often act as ideal electrode materials for the development of PEC biosensors due to their structure features, such as π-electron conjugation, low band gap, and active groups.[41,42] Further, metal tetra-amine phthalocyanine (M-TAPc, M = Cu, Zn, or Co), phthalocyanine derivatives, not only display highly efficient photoelectrochemical properties but also can be utilized as building blocks for the synthesis of COFs.[43,44] Thereby, the exploration of the Pc-based COFs as the PEC sensor platforms is expected. Most recently, MOF@COF heterostructures, which are prepared by diverse combination types of MOFs and COFs, i.e., core−shell MOF@COF or COF@MOF and MOF-on-COF, have emerged as hybrid architectures.[45] The MOF@COF hybrids can effectively integrate unique advantages of their parents, producing novel porous nanomaterials with outperformed physicochemical properties.[46,47] By integrating the aromaticity of MOFs and the ordered pillar−columnar structure characteristics of COFs, the fabricated MOF@COF hybrid materials display a strong $\pi-\pi$ stacking interaction, overcoming the inherent disadvantages of sole MOFs and COFs and resulting in a synergistic effect to provide multifunctional properties for specific and personalized applications. Diverse MOF@COF heterostructures have been developed and used as catalysts,[48−51] gas adsorbents,[52] supercapacitors,[53] and biosensors.[54,55] A Co-MOF@TPN-COF nanoarchitecture has been developed and exploited as novel platforms for an oxytetracycline aptasensor, giving an extremely low LOD of 0.217 fg mL^{-1} detected by the electrochemical technique,[54,55] much lower than the biosensors for detecting oxytetracycline using other nanomaterials as platforms.[56,57] Thus far, however, there is no report on the construction of the dual-mode PEC−EC biosensors for the detection of HIV-1 based on the core−shell MOF@COF hybrids with $\pi-\pi$ stacking interaction and sizable specific surface.

In light of the integrated advantages of MOF@COF heterostructures and high sensing performances of PEC and EC techniques, we aim to design and construct a novel MOF@COF hybrid architecture and develop it as a bifunctional sensitive platform for a dual-mode PEC−EC biosensor via the

https://doi.org/10.1021/acs.langmuir.1c02253
Langmuir 2021, 37, 13479−13492

Scheme 1. (a) Preparation of the Cu-MOF@CuPc-TA-COF Hybrid Material and (b) Construction Procedure of the HIV-1 DNA Biosensor Based on the Cu-MOF@CuPc-TA-COF Hybrid

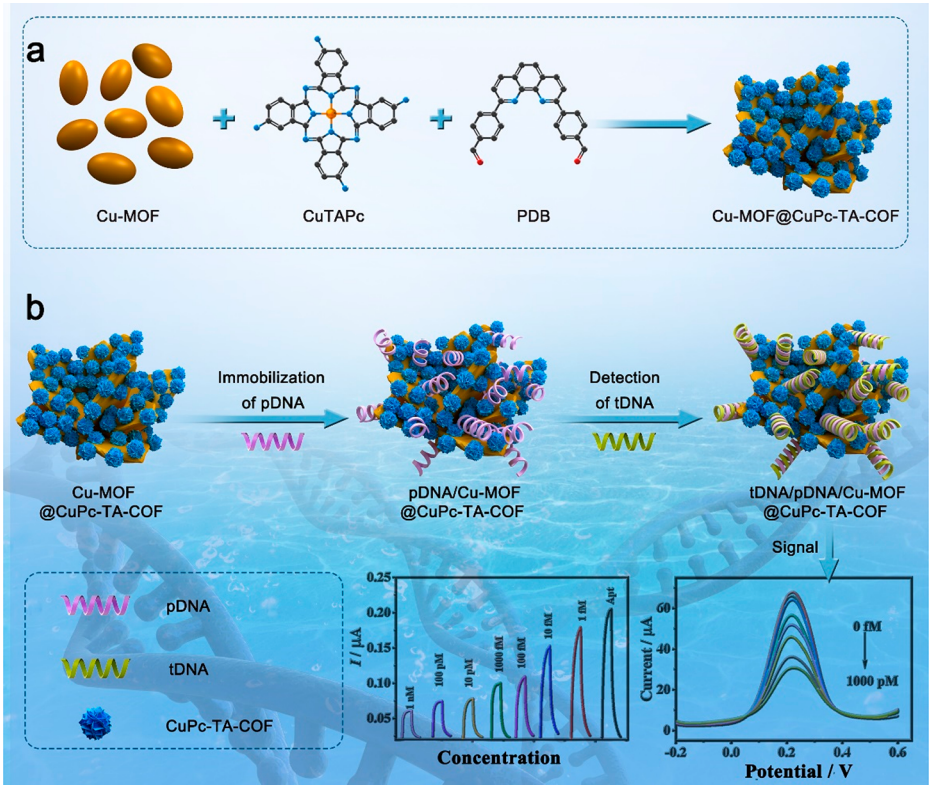

efficient immobilization of the HIV-1-targeted DNA probe. The developed MOF@COF-based biosensor was then employed to detect HIV-1 DNA via the hybridization between the DNA probe and HIV-1 target DNA by the dual-mode PEC−EC approach (Scheme 1). Using the presynthesized ellipsoidal copper-based MOF (Cu-MOF) as a template, the new structured COF was prepared using copper-phthalocyanine tetra-amine (CuTAPc) and 2,9-bis[*p*-(formyl)phenyl]-1,10-phenanthroline (PDB) as building blocks via the Schiff base condensation between amino and carbonyl groups, thus forming the Cu-MOF@CuPc-TA-COF hybrid (Scheme 1a). Benefiting from the high bioaffinity of Cu-MOF and CuTAPc-COF toward the probe DNA strands, excellent photoactivity and good electrochemical activity of Cu-MOF, and the synergistic effect between the two components, the Cu-MOF@CuPc-TA-COF-based PEC−EC biosensor, respectively, demonstrates an extremely low LOD of 0.07 and 0.18 fM for PEC and EC techniques within the HIV-1 target DNA concentration from 1 fM to 1 nM, which are remarkably lower than the reported HIV-1 biosensors. Moreover, due to good stability of the synthesized hybrid in aqueous solution, the developed biosensor illustrates superior sensing performances toward HIV-1 target DNA, such as remarkable selectivity, high stability, good reproducibility, and preferable regeneration ability, as well as acceptable applicability. The developed PEC−EC-based biosensors via the combination of PEC and EC techniques exhibit three advantages: (i) Dual-mode detection could provide two kinds of response signals, which benefit the elimination of the environment influences and uncontrollable variability. (ii) Based on different signal transduction mechanisms, the PEC−EC sensing approach can improve the reliability of detection results, efficiently supporting the accurate analysis. (iii) The PEC−EC dual-mode biosensor based on MOF@COF with good photoactivity and electroactivity can be feasibly constructed. Therefore, the present work not only provides a new construction of the MOF@COF architecture but also makes a deep insight into a new sensing strategy for detecting HIV-1 DNA by PEC and EC techniques, which further widely extends the application of the MOF@COF heterostructures in the biomedical field.

2. EXPERIMENTAL SECTION

Section S1 (Supporting Information) provides the description of reagents and materials, preparation of Cu-MOF, CuPc-TA-COF, and all solutions, pretreatment of the glass carbon electrode (GCE), basic characterizations, and PEC and EC measurements. The sequences of the used probe DNA and target DNA of HIV-1 are shown as follows:

Probe DNA (pDNA): 5′-GGGGGGCCAAGGCCCAGCC-CTCACACA-3′

Target DNA (tDNA): 5′-TGTGTGAGGGCTGGGCCTTGG-3′

2.1. Synthesis of the Cu-MOF@CuPc-TA-COF Heterostructure and CuPc-TA-COF. Typically, CuPc-TA (0.05 mmol), 2,9-bis[*p*-(formyl)phenyl]-1,10-phenanthroline (PDB) (0.1 mmol), and Cu-MOF (30 mg) were successively dispersed in 10 mL of dimethyl sulfoxide. Afterward, 50 μL of acetic acid was added and acted as a catalyst. After ultrasonication for 5 min, the reaction was kept in an oil bath at 120 °C for 72 h after three freeze−thaw cycles. Finally, the Cu-MOF@CuPc-TA-COF heterostructure can be obtained after drying under a vacuum at 70 °C. For a comparison, the CuPc-TA-COF was also synthesized using a similar method, but without adding Cu-MOF. In addition, the chemical component of CuPc-TA-COF was analyzed by a solid state ^{13}C NMR (nuclear magnetic resonance) spectrum (Figure S2). The signal located at 160 ppm is assigned to the C═N group, and the signals at 125 and 136 ppm correspond to the carbon atoms of the phthalocyanine and phenyl groups.[58] Moreover, the signals at 141 ppm are ascribed to the carbon atoms

https://doi.org/10.1021/acs.langmuir.1c02253
Langmuir 2021, 37, 13479−13492

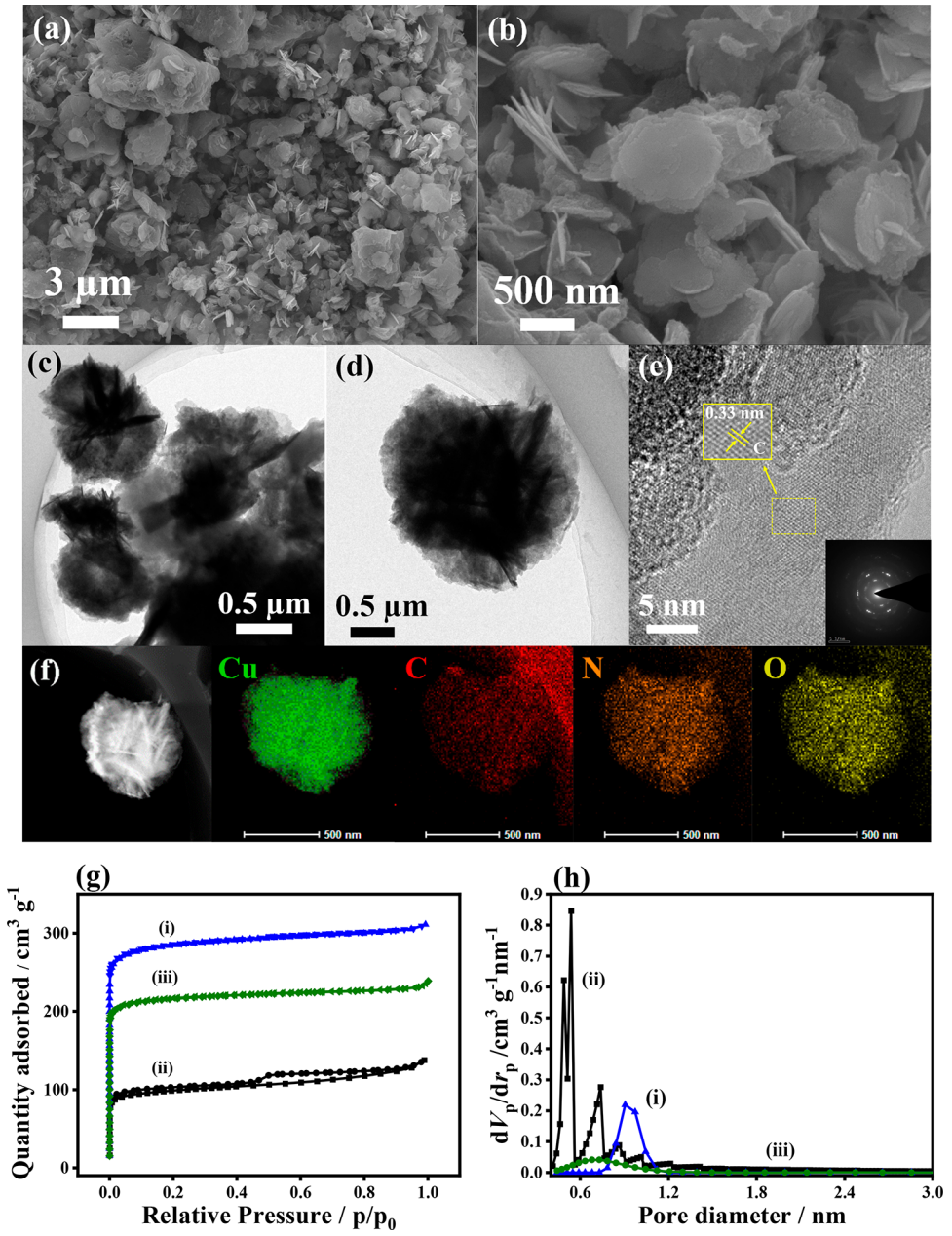

Figure 1. (a, b) Low- and high-magnification SEM. (c–e) Low- and high-magnification and HR-TEM images. (f) Element mapping distribution of Cu (green), C (red), N (brown), and O (yellow) of the Cu-MOF@CuPc-TA-COF hybrid. (g) Nitrogen adsorption–desorption isotherms and (h) distribution of pore diameters of (i) Cu-MOF, (ii) CuPc-TA-COF, and (iii) Cu-MOF@CuPc-TA-COF.

neighboring the imine bonds. The other signals originate from the solvent during the synthesis procedure.[59] Therefore, this result indicates that the CuPc-TA-COF has been prepared as expected. Furthermore, no unexpected or unusually high safety hazards were encountered.

2.2. Fabrication of the Cu-MOF@CuPc-TA-COF-Based Biosensor for Detecting tDNA. The different dosages of the Cu-MOF@CuPc-TA-COF hybrid (1, 2, 5, 10, 15, and 20 mg) were separately dispersed in 10 mL of deionized water to form the different concentrations of the hybrid suspensions (0.1, 0.2, 0.5, 1, 1.5, and 2 mg mL^{-1}). Then, they were used for the modification of the GCE to investigate the effect of the dosage of the hybrid on the sensing performance. Subsequently, the homogeneous Cu-MOF@CuPc-TA-COF suspension (10 μL) was dropped onto the treated GCE surface and dried at room temperature, followed by rinsing thoroughly with water to remove the loose adhered hybrid (represented by Cu-MOF@CuPc-TA-COF/GCE). After that, the Cu-MOF@CuPc-TA-COF/GCE was incubated by pDNA solution for 1 h, followed by washing with phosphate buffer solution (PBS, 0.1 M, pH = 7.4) thoroughly to remove the weak adsorbed pDNA strands (represented by pDNA/Cu-MOF@CuPc-TA-COF/GCE). Here, different concentrations of pDNA solutions (10, 20, 50, 100, and 200 nM) were used to assess the influence of the concentration of pDNA on the detection of the tDNA. Finally, the proposed pDNA/Cu-MOF@CuPc-TA-COF/GCE was incubated with tDNA solution (1 fM) at different time intervals (10, 20, 30, 40, 50, 60, 70, and 80 min) (denoted as tDNA/pDNA/Cu-MOF@CuPc-TA-COF/GCE) for probing the effect of the binding time of tDNA on the detection result. For a comparison, the Cu-MOF- and CuPc-TA-COF-based biosensors were also constructed by analogous procedures. All biosensors or electrodes were stored in a refrigerator (4 °C) when not used.

2.3. Analytical and Sensing Performances of HIV-1 Based on the Developed Cu-MOF@CuPc-TA-COF-Based Biosensor. The parameter options of PEC and EC measurements are provided in

https://doi.org/10.1021/acs.langmuir.1c02253
Langmuir 2021, 37, 13479–13492

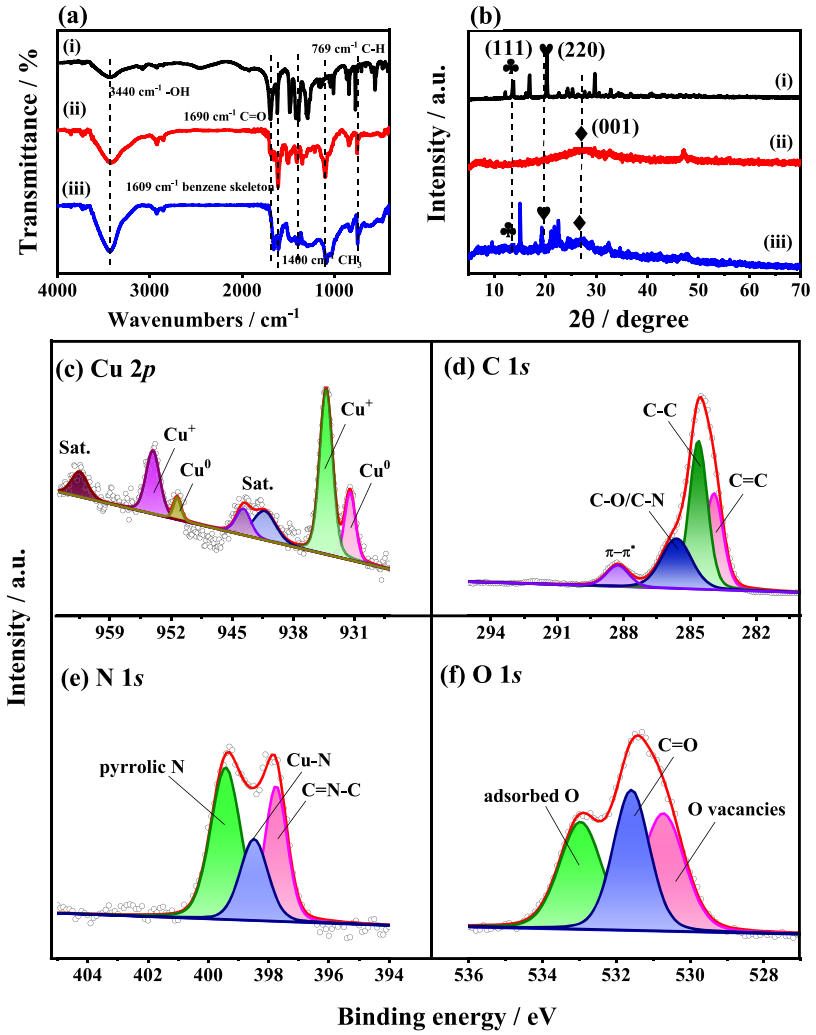

Figure 2. (a) FT-IR spectra and (b) XRD patterns of (i) Cu-MOF, (ii) CuTAPc-COF, and (iii) the Cu-MOF@CuPc-TA-COF hybrid. High-resolution (c) Cu 2p, (d) C 1s, (e) N 1s, and (f) O 1s XPS spectra of the Cu-MOF@CuPc-TA-COF hybrid.

Section S1.8 and Figure S3 (Supporting Information). Here, all determination conditions of EC and PEC methods for the sensing performances of the developed biosensor are the same. The quantitative analysis of tDNA was carried out for recording the EC and photocurrent responses of the tDNA/pDNA/Cu-MOF@CuPc-TA-COF/GCE when separately incubated with different concentrations of tDNA solutions (1 fM, 10 fM, 100 fM, 1 pM, 10 pM, 100 pM, and 1 nM). The calibration curve was obtained when taking the photocurrent responses or electrochemical signals as the function of the logarithm of the concentration of tDNA. Afterward, the LOD of the developed biosensor was deduced from the calibration curve according to IUPAC.[60]

For assessing the selectivity of the constructed biosensor, noncomplementary DNA (nc-DNA), two mismatched DNA (MM2-DNA), Ca^{2+}, Na^{+}, K^{+}, urea, uric acid, α-fetoprotein (AFP), carcinoembryonic (CEA), and mucin 1 (MUC1) with the concentration of 0.1 pM, which was 100-fold the concentration of tDNA (1 fM), were applied as interferents. In addition, five individual pDNA/Cu-MOF@CuPc-TA-COF/GCE were utilized for the detection of tDNA (1 fM) to test the reproducibility. The responses of the obtained tDNA/pDNA/Cu-MOF@CuPc-TA-COF/GCE were continuously measured for 15 days to assess the stability. Further, the applicability of the proposed biosensor was tested by detecting tDNA, which was spiked into human serum (obtained from Solarbio life sciences) and diluted to different concentrations of HIV-1 DNA (1 fM, 10 fM, 100 fM, 1 pM, 10 pM, 100 pM, and 1 nM). Meanwhile, the real-time fluorescent quantitative polymerase chain reaction (RT-qPCR) was employed to evaluate the accuracy of the proposed biosensor, in which a commercially available careHIV-1 RT-PCR assay was used.

3. RESULTS AND DISCUSSION

3.1. Basic Characterizations of Cu-MOF, CuPc-TA-COF, and the Cu-MOF@CuPc-TA-COF Hybrid. The surface morphologies and nanostructures of the Cu-MOF@CuPc-TA-COF hybrid were probed by field emission scanning electron microscopy (FE-SEM) and high-resolution transmission electron microscopy (HR-TEM) techniques. The surface structures of Cu-MOF and CuPc-TA-COF are also analyzed (see Figures S4 and S5). The SEM image of the Cu-MOF@CuPc-TA-COF hybrid (Figure 1a) shows that it has a nanoflower shape, which is assembled with multilayered nanoflakes with a rough surface (Figure 1b). This lamellar stacking structure of the Cu-MOF@CuPc-TA-COF hybrid can facilitate the pDNA immobilization.[61] Meanwhile, it is apparent that the hybrid of Cu-MOF and CuPc-TA-COF is largely different from individual Cu-MOF and CuPc-TA-COF, which could be due to the fact that they have intimate interfacial contact, leading to the change of Cu-MOF nanoellipsoids and CuPc-TA-COF. Therefore, it can be concluded that the CuPc-TA-COF grew on the Cu-MOF

https://doi.org/10.1021/acs.langmuir.1c02253
Langmuir 2021, 37, 13479−13492

nanoellipsoid, forming the protection layer for Cu-MOF during the preparation of the Cu-MOF@CuPc-TA-COF hybrid. Therefore, the hybrid shows the nano-flower-like structure fabricated by a stacking nanolayer. Furthermore, the TEM image of the Cu-MOF@CuPc-TA-COF hybrid (Figure 1c,d) is composed of irregular nanoparticles, suggesting that the nano-flower-like structure is assembled of particles. It is noteworthy that the Cu-MOF stands vertically on the surface of Cu-MOF@CuPc-TA-COF hybrids. The HR-TEM image of the hybrid (Figure 1e) shows that the edge of the Cu-MOF@CuPc-TA-COF hybrid is capped by a carbon substrate with the characteristic *d*-spacing of 0.33 nm, which is ascribed to the $\pi-\pi$ stacking of CuPc-TA-COF. Moreover, the *d*-spacing corresponds to the diffraction peak of (001).[62] Further, the energy-dispersive spectroscopy (EDS) mappings (Figure 1f) reveal the homogeneous distribution of Cu, C, N, and O elements contained in the prepared hybrid.

The Brunauer−Emmett−Teller (BET) specific surface areas of all samples were measured (Figure 1). As shown in Figure 1g, the Cu-MOF@CuPc-TA-COF displays a typical type I isotherm with a dramatic nitrogen adsorption at a low relative pressure ($P/P_0 < 0.05$) and no hysteresis loops on the isotherm indicating the emblematic microporous structure of Cu-MOF@CuPc-TA-COF. Table S1 indicates that Cu-MOF@CuPc-TA-COF has the largest BET surface area of 514.7 $m^2\ g^{-1}$ in comparison with Cu-MOF (311.8 $m^2\ g^{-1}$) and CuPc-TA-COF (446.03 $m^2\ g^{-1}$). The pore size distribution was calculated by a DFT simulation (Figure 1h). The average pore diameters of Cu-MOF@CuPc-TA-COF, Cu-MOF, and CuPc-TA-COF were 1.97, 2.74, and 2.25 nm, respectively. The Cu-MOF@CuPc-TA-COF has a large specific surface area and small average pore size, indicting its abundant pore structure, which can provide more activity sites benefiting its use as a scaffold for the immobilization of probe DNA. The large specific surface area of the porous structure can provide more activity sites to anchor more probe DNA.[63]

The chemical features and crystal structures of Cu-MOF, CuPc-TA-COF, and Cu-MOF@CuPc-TA-COF were investigated by Fourier transform infrared spectroscopy (FT-IR), X-ray photoelectron spectroscopy (XPS), and powder X-ray diffraction measurements (PXRD) techniques. The FT-IR spectrum of Cu-MOF (curve i, Figure 2a) illustrates the absorption bands at 1690 and 1615 cm^{-1}, which are ascribed to the stretching vibrations of the carbon−oxygen double bond (C═O) in the carboxyl group (—COOH) and benzene skeleton vibration, respectively. As for CuPc-TA-COF (curve ii, Figure 2a), the peaks at 1609 and 1623 cm^{-1} belong to the benzene skeleton vibration and N—H bending vibration, respectively. Moreover, the adsorption peak at 1660 cm^{-1} is assigned to C═N stretching, proving the formation of M-Pc and the reaction with PDB. After the integration of CuPc-TA-COF and Cu-MOF (curve iii, Figure 2a), there was no substantial change in the FT-IR spectra in comparison with those of CoPc-TA-COF, suggesting that the Cu-MOF was embedded by the CuPc-TA-COF layer, which is consistent with the PXRD result. The PXRD pattern of Cu-MOF (Figure 2b) displays the main characteristic peaks at 2θ = 13.7°, 16.9°, 20.3°, and 29.7°, consistent with the reported literature.[64] The PXRD pattern of CuPc-TA-COF shows a broad diffraction peak at 26.3°, which is assigned with the amorphous graphitic structure and reflection from the planes of (001).[62] This finding reveals its weak crystallinity, which is consistent with the TEM result. As for the Cu-MOF@CuPc-TA-COF hybrid, the PXRD pattern comprises the diffraction peaks of two components of Cu-MOF and CuPc-TA-COF, hinting at their combination.

XPS measurements were also carried out for determining the chemical environment and structure of all samples. Figure S6 indicates the XPS survey spectra of Cu-MOF, CuTAPc-COF, and the Cu-MOF@CuPc-TA-COF hybrid, confirming the coexistence of C 1s (284.6 eV), O 1s (531 eV), N 1s (400 eV), and Cu 2p (934 eV) signals. The individual region of each element was analyzed by fitting their corresponding high-resolution XPS spectra with XPSPEAK1 software, which were used for studying their chemical structures and components for the three samples (Figure 2 and Figure S3). As for the Cu-MOF@CuPc-TA-COF hybrid, the deconvoluted spectrum of the high-resolution Cu 2p XPS (Figure 2c) can be separated into the two major peaks at the binding energies (BEs) of 935.5 and 955.4 eV attributed to Cu $2p_{3/2}$ and Cu $2p_{1/2}$, respectively. The Cu $2p_{3/2}$ component includes four components at the BEs of 931.5, 934.2, 941.3, and 943.7 eV, corresponding to the Cu metal state (Cu^0), Cu^+, and their satellite peaks. The similar parts are also observed in the Cu $2p_{1/2}$ part. This indicates that the added Cu^{2+} species were reduced to their low valence states (Cu^0/Cu^+) during the preparation of the Cu-MOF@CuPc-TA-COF hybrid. The mixed metal valence states of copper ions can facilitate both the electroactivity and photoactivity of the developed hybrid.[65] In terms of the high-resolution C 1s XPS spectrum (Figure 2d), it is deconvoluted into C═C (283.9 eV), C—C (284.6 eV), C—N/C—O (285.6 eV), and $\pi-\pi^*$ (288.3 eV). Among these, the content of C═C hints at its highly conjugated chemical structure, improving the electrochemical activity of the hybrid.[66] The high-resolution N 1s XPS spectrum (Figure 2e) can be divided into the three peaks at the BEs of 398.5, 397.8, and 399.4 eV, which are assigned with the sp^2-hybridized aromatic nitrogen (C═N—C), Cu—N, and pyrrolic N, respectively. Among them, Cu—N moieties are due to the presence of CuPc rings. The clear O 1s spectrum (Figure 2f) can be fitted to O vacancies (530.7 eV), C═O (531.6 eV), and adsorbed O (533 eV), in which the high content of O vacancies contained in the hybrid can remarkably boost electron transfer and enhance photoactivity.[67] Moreover, the detailed XPS spectra of each element contained in Cu-MOF and CuPc-TA-COF were also analyzed (Figure S7).

Furthermore, prior to the investigation on the pDNA immobilization using PEC and EC measurements, the change in the chemical structure and components before and after pDNA strands over the Cu-MOF@CuPc-TA-COF hybrid was also evaluated by XPS characterization. As displayed in the Cu 2p XPS spectrum of the pDNA/Cu-MOF@CuPc-TA-COF complex (Figure S8a), besides Cu^0 and Cu^+ species, a small peak at the BE of 936.2 eV, due to Cu^{2+} of Cu $2p_{3/2}$, is also observed, suggesting that a partial Cu^+ species was oxidized during the DNA immobilization procedure. In terms of the C 1s XPS spectrum (Figure S8b), apparent peaks of C═O (287.1 eV), COO/N—C═O (292.4 eV), and K^+ (295.4 eV) can be obtained, apart from C═C, C—C, C—N/C—N, and $\pi-\pi^*$. Among these, C═O and COO/N—C═O groups originate from the immobilized oligonucleotide strands, while K^+ is obtained from the PBS solution. This hints at the successful immobilization of the DNA probe over the hybrid. The high-resolution N 1s spectrum (Figure S8c) can be fitted to two main parts of Cu—N and pyrrolic N, along with the weak peaks of graphitic N (400.9 eV) and NO_x (403.7 eV). As

https://doi.org/10.1021/acs.langmuir.1c02253
Langmuir 2021, 37, 13479−13492

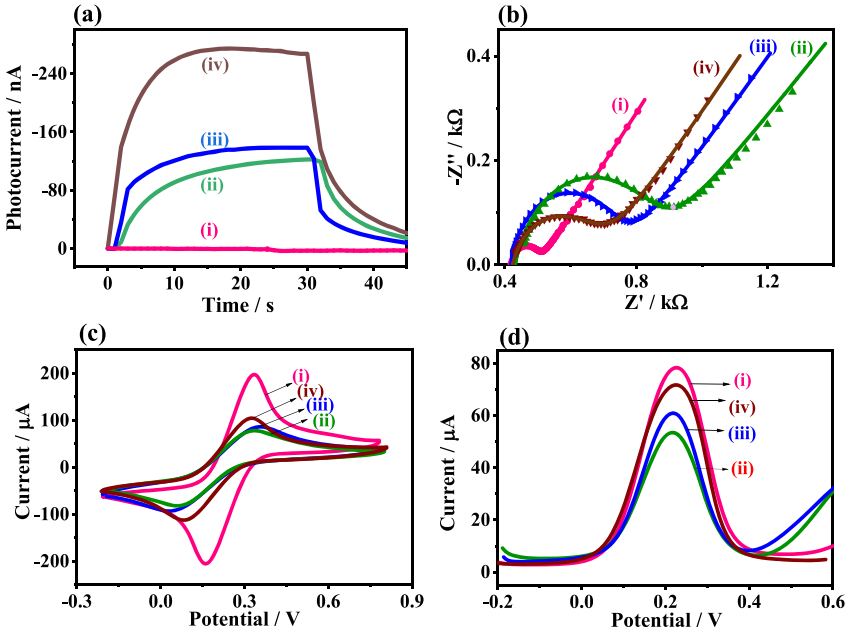

Figure 3. (a) Photocurrent in PBS (0.1 M, pH = 7.4), (b) EIS Nyquist plots, (c) CV curves, and (d) DPV plots in PBS (0.1 M, pH = 7.4) containing 5 mM $[Fe(CN)_6]^{3-/4-}$ solution and 0.1 M KCl, responses of different modified electrodes: (i) GCE, (ii) Cu-MOF/GCE, (iii) CuPc-TA-COF/GCE, and (iv) Cu-MOF@CuPc-TA-COF/GCE.

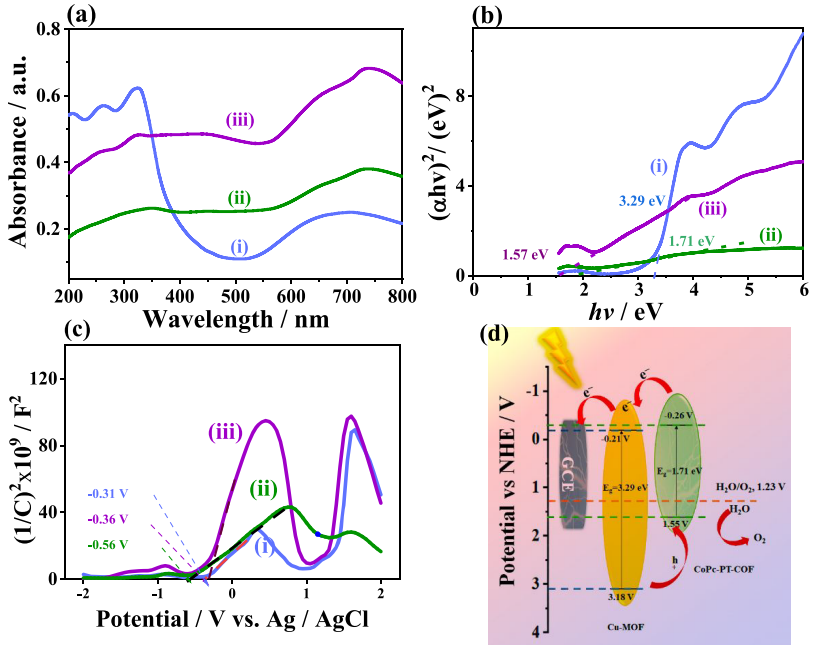

Figure 4. (a) UV−vis DRS, (b) plots of $(\alpha h\nu)^2$ versus energy ($h\nu$), and (c) Mott−Schottky plots of (i) Cu-MOF, (ii) CuPc-TA-COF, and (iii) Cu-MOF@CuPc-TA-COF. (d) Schematic diagram of the energy band structure of the Cu-MOF@CuPc-TA-COF heterojunction.

compared with the pristine Cu-MOF@CuPc-TA-COF hybrid, the peak content of the Cu—N moiety increases, revealing the coordination of Cu ions with nitrogen bearing on oligonucleotide strands. Also, graphitic N is due to the immobilized DNA probe, while a small partial N component was oxidized. An additional peak of C—O (532.6 eV) is observed in the O 1s XPS spectrum (Figure S8d). Notably, the clear P 2p XPS signal (Figure S8e) is obtained in the pDNA/Cu-MOF@CuPc-TA-COF complex, which is ascribed to the phosphate group contained in the DNA probe. The P 2p XPS spectrum can be deconvoluted into two parts of P $2p_{3/2}$ and P $2p_{1/2}$ at 132.5 and 133.4 eV, respectively. These results hint that the pDNA strands can strongly immobilize over the proposed Cu-MOF@CuPc-TA-COF, thus showing the great potential for manufacturing the HIV-1 biosensor.

3.2. Evaluation of PEC and EC Performances for Cu-MOF, CuPc-TA-COF, and the Cu-MOF@CuPc-TA-COF Hybrid. The electrochemical performances of Cu-MOF, CuPc-TA-COF, and the Cu-MOF@CuPc-TA-COF hybrid were separately investigated by photoelectrochemical (PEC), electrochemical impedance spectroscopy (EIS), cyclic voltammetry (CV), and differential pulse voltammetry (DPV)

https://doi.org/10.1021/acs.langmuir.1c02253
Langmuir 2021, 37, 13479−13492

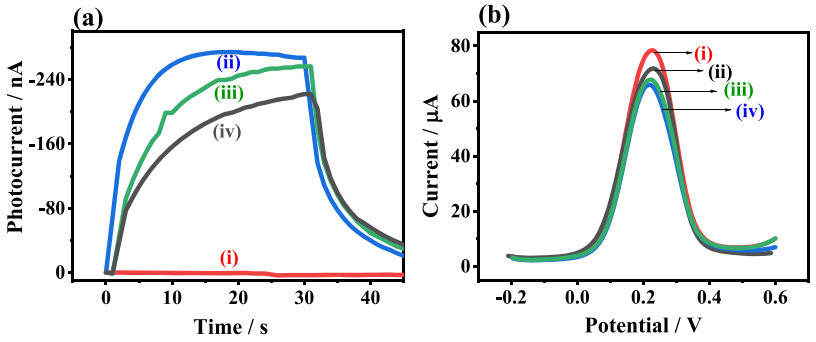

Figure 5. (a) Photocurrent responses and (b) DPV curves of (i) the GCE, (ii) Cu-MOF@CuPc-TA-COF, (iii) pDNA/Cu-MOF@CuPc-TA-COF, and (iv) tDNA/pDNA/Cu-MOF@CuPc-TA-COF.

techniques (Figure 3). The photocurrents of the three samples were tested by PEC (Figure 3a), in which the bare GCE shows a negligible photocurrent (curve i). As compared, the PEC signal of the Cu-MOF@CuPc-TA-COF electrode gives a photocurrent (curve iv, 258 nA), substantially higher than those of Cu-MOF (127 nA, curve ii) and CuPc-TA-COF (139 nA, curve iii). This indicates that the heterojunction structure of the Cu-MOF@CuPc-TA-COF hybrid can effectively improve the photoactivity by integrating Cu-MOF and CuPc-TA-COF, which can further facilitate the detection sensitivity toward the detection of HIV-1 DNA.

Figure 3b indicates that the bare GCE only gives a small resistance of charge transfer (R_{ct}) value 30.9 Ω, which is due to its excellent electrochemical activity. After separately modifying the GCE with Cu-MOF, CuPc-TA-COF, and the Cu-MOF@CuPc-TA-COF hybrid, the Cu-MOF/GCE, CuPc-TA-COF/GCE, and Cu-MOF@CuPc-TA-COF/GCE display the R_{ct} values of 404.2, 265.4, and 181.3 Ω, respectively, larger than that of the bare GCE. The increase of the R_{ct} values of the modified GCE suggests the relatively weak electrochemical performances of all samples. Among them, the Cu-MOF@CuPc-TA-COF/GCE has the smallest R_{ct} value, hinting at its superior electrochemical activity to their parents. These results can be proven by their corresponding CV and DPV curves. As demonstrated in the CV curves (Figure 3c), the bare GCE shows the corresponding redox behavior at a fixed scan rate of 50 mV s^{-1}, showing the broad peak potential separation (ΔE) of 0.17 V and high peak current density (ΔI) of 402.10 μA due to the $[Fe(CN)_6]^{3-/4-}$ probe. The Cu-MOF@CuPc-TA-COF/GCE exhibits the ΔE of 0.23 V, narrower than those of the Cu-MOF/GCE (ΔE = 0.27 V) and CuPc-TA-COF/GCE (ΔE = 0.33 V), along with a larger I_p (217.23 μA) than those of the Cu-MOF/GCE (ΔI = 155.60 μA) and CuPc-TA-COF/GCE (ΔI = 182.47 μA). These findings hint at the outperformed electrochemical activity of the proposed Cu-MOF@CuPc-TA-COF hybrid to Cu-MOF and CuPc-TA-COF. Meanwhile, the DPV curves of all samples (Figure 3d) show that the peak current of the bare GCE is as large as 78.4 μA. After separately modifying with Cu-MOF, CuPc-TA-COF, and Cu-MOF@CuPc-TA-COF, the peak current of the electrode slightly decreases, suggesting that the presence of these materials somehow hampers the electron transfer at the electron/electrolyte interface. Among these, the Cu-MOF@CuPc-TA-COF/GCE also shows the largest peak current (curve iv, 71.7 μA), larger than those of Cu-MOF/GCE (curve ii, 53.5 μA) and CuPc-TA-COF/GCE (curve iii, 60.9 μA), revealing its superior EC performance.

For a deep understanding of the improved electrochemical activity and photoactivity of the Cu-MOF@CuPc-TA-COF hybrid material, the basic photoelectrical performance was investigated. Figure 4a shows the UV−vis diffuse reflectance spectra (DRS) of all samples. The UV−vis DRS spectrum of the pristine Cu-MOF displays an obvious absorption edge of 350−400 nm, while the Cu-MOF@CuPc-TA-COF and CuPc-Ta-COF also show a weak adsorption range 350−400 nm. Further, they all show an enhanced visible light absorption within the light range 550−780 nm. In addition, according to the Tauc plot (calculated by the plot of $(\alpha h\upsilon)^n$ versus $h\upsilon$, where the n = 2 represents direct-gap semiconductors and n = 1/2 represents indirect-gap semiconductors)[68] (Figure 4b), the band gap energy (E_g) of the Cu-MOF@CuPc-TA-COF hybrid is the narrowest (1.57 eV) among the three samples, while those of the Cu-MOF and CuPc-TA-COF are 3.29 and 1.71 eV, respectively. The narrow band gap demonstrates that the obtained Cu-MOF@CuPc-TA-COF possesses the enhanced visible light harvesting ability, which can remarkably increase the efficient utilization of solar energy.

Meanwhile, the Mott−Schottky measurements (Figure 4c) indicate that the Cu-MOF and CuPc-TA-COF are an n-type semiconductor. Therefore, the flat band potentials (E_{fb}) of Cu-MOF and CuPc-TA-COF are approximately −0.11 and −0.16 V (vs normal hydrogen electrode (NHE)) according to the Nernst equation, respectively. Further, the potential of the lowest unoccupied molecular orbital (LUMO) is 0.1−0.2 V more negative than E_{fb} for the n-type semiconductor. Hence, the E_{LUMO} values of Cu-MOF and CuPc-TA-COF are −0.21 and −0.26 V, respectively.[22,69] The highest occupied molecular orbital (E_{HOMO}) potential can be obtained from the equation $E_{HOMO} = E_{LUMO} + E_g$. Consequently, the E_{HOMO} values of Cu-MOF and CuPc-TA-COF are 3.18 and 1.55 V, respectively. As aforementioned, the schematic illustration of the band structure of Cu-MOF and CuPc-TA-COF is shown in Figure 4d. It indicates that the electrons can migrate from the LUMO of Cu-MOF to that of CuPc-TA-COF based on the energy band match. Furthermore, the hole generated at Cu-MOF can be consumed by H_2O according to the potential of H_2O/O_2 (+1.23 V vs NHE),[63] which would decrease the efficiency of electron−hole recombination, gaining the enhanced PEC response.

3.3. Electrochemical Sensing Performances of the Developed Biosensor. Given that the Cu-MOF@CuPc-TA-COF hybrid possesses the superior electrochemical performance and photoactivity as compared to its parents, it was chosen as the platform for anchoring pDNA to manufacture the PEC−EC biosensor for detecting tDNA. The PEC

https://doi.org/10.1021/acs.langmuir.1c02253
Langmuir 2021, 37, 13479−13492

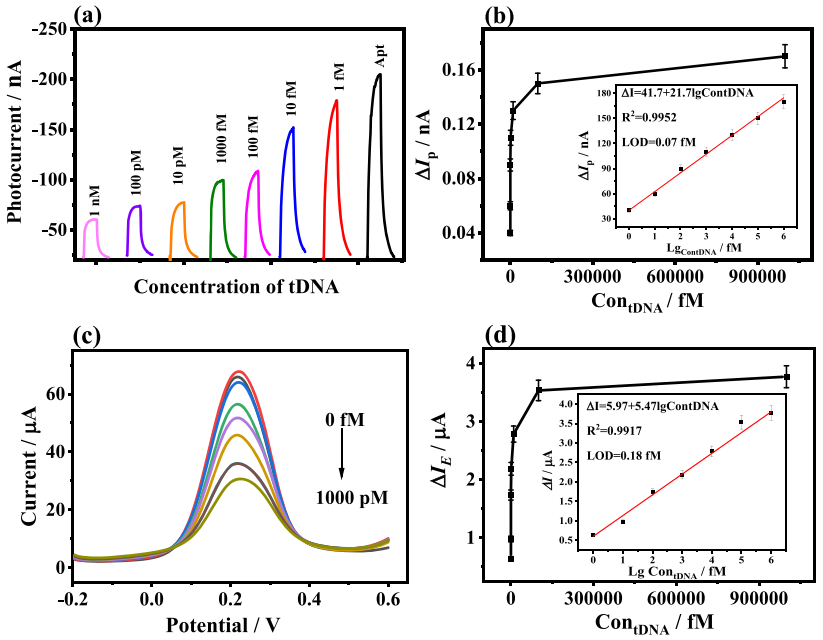

Figure 6. (a) Photocurrent responses. (b) Calibration curve of the PEC biosensor. (c) DPV plots for the detection of tDNA at different concentrations (1 fM, 10 fM, 100 fM, 1 pM, 10 pM, 100 pM, and 1 nM) using the Cu-MOF@CuPc-TA-COF-based biosensor. (d) Calibration curves between ΔI_E and tDNA concentrations (inset: the linear fit plot of ΔI_E as a function of the logarithm of tDNA concentration, where the error bars are standard deviations for n = 3). The error bars show the standard deviation of five replicate determinations.

technique was used to detect the fabrication procedure of the biosensor and detection of tDNA (Figure 5a). The anchoring efficiency of pDNA and detection sensitivity of tDNA using the Cu-MOF@CuPc-TA-COF-based biosensor were evaluated using the relative changes in their photocurrent densities values (ΔI), which was represented as $\Delta I_p = I_{p,i+1} - I_{p,i}$ associated with each step of pDNA immobilization and tDNA detection. After the pDNA immobilization, the pDNA/Cu-MOF@CuPc-TA-COF-based biosensor shows the ΔI value of 17.7 nA, displaying a superior anchoring ability toward pDNA. After the analysis of HIV-1 DNA, the pDNA/Cu-MOF@CuPc-TA-COF/GCE also demonstrates the substantial hybridization ability, giving a ΔI value of 34.5 nA. As aforementioned, the CuPc-TA-COF/GCE exhibits a relatively good photoactivity. After anchoring the pDNA on the hybrid, electrons move slowly due to the block effect of pDNA. Furthermore, the electron migration is further obstructed when tDNA binds with pDNA.

In addition, Figure 5b shows the DPV curves of the construction of the biosensor based on the Cu-MOF@CuPc-TA-COF hybrid and detection of tDNA. After immobilizing pDNA strands over the modified GCE, the peak current of the pDNA/Cu-MOF@CuPc-TA-COF/GCE (curve iii) continuously decreases to 67.76 μA, demonstrating that insulated DNA strands can improve the steric hindrance and hinder the access of the redox probe to the electrode surface.[70] Additionally, negative charges bearing on the pDNA oligonucleotide strands can cause the apparent repulsion with $[Fe(CN)_6]^{3-/4-}$, hampering electron transfer at the interface of the electron/electrolyte. After the detection of tDNA, the peak current further decreases to 65.86 μA (curve iv) owing to the formation of the double DNA strand helix, strengthening the steric hindrance. Moreover, the double stranded nucleotides bear more negatively charged phosphate groups, leading to the strong repulsion with the $[Fe(CN)_6]^{3-/4-}$ probe. It thus results in the decline of the peak current of the modified electrode, proving the successful hybridization between pDNA and tDNA strands. These results are consistent with the CV measurements, for which the peak current of the electrode continuously decreases for the pDNA immobilization and detection of tDNA (Figure S12a). The construction and detection procedure of the biosensor was also assessed by the EIS technique (Figure S12b). The R_{ct} of the pDNA/Cu-MOF@CuPc-TA-COF/GCE increases to 364.2 Ω, while the tDNA/pDNA/Cu-MOF@CuPc-TA-COF/GCE becomes even larger (565.9 Ω).

For obtaining a remarkable detection performance, the sensing determination parameters were optimized prior to the detection of tDNA (Section S4, Supporting Information). The optimal conditions for fabricating the PEC−EC biosensor or detecting tDNA according to the PEC technique are summarized as follows: the usage of the Cu-MOF@CuPc-TA-COF suspension of 1 mg mL^{-1} for the modification of the electrode, the pDNA concentration of 100 nM, the incubation time of pDNA strands of 1 h, and the binding time of pDNA and tDNA of 40 min.

3.4. Quantitative Analysis of tDNA Using the Cu-MOF@CuPc-TA-COF-Based Biosensor. Under the optimized conditions, the responses of pDNA/Cu-MOF@CuPc-TA-COF/GCE with different tDNA concentrations were recorded by PEC and DPV approaches, respectively. Figure 6a demonstrates the caused change in the photocurrent density for detecting tDNA using the proposed biosensor decreases with increasing the tDNA concentration, of which the tDNA concentration was varied from 1 fM to 1 nM. The photocurrent variation ($\Delta I_p = I_{p,0} - I_p$, $I_{p,0}$ and I_p are the photocurrents of the pDNA/Cu-MOF@CuPc-TA-COF/GCE before and after interacting with tDNA, respectively) reflects the hybridization of tDNA and pDNA using the developed PEC biosensor. Clearly, there is a good linear relationship between the logarithm of tDNA concentration [$lgCon_{tDNA}$ (fM)] and the obtained ΔI, for which there is an equation of

https://doi.org/10.1021/acs.langmuir.1c02253
Langmuir 2021, 37, 13479−13492

Table 1. Comparison with Other Reported Techniques for HIV-1 DNA Detection

materials	detection method	detection range	LOD (fM)	refs
$NiCo_2O_4$/CoO@CNTs	EIS	0.1 pM to 20 nM	16.7	71
CdTe QDs and poly[G]/S-NPs	PEC	10 ng mL^{-1} to 10 mg mL^{-1}	10 ng mL^{-1}	72
β-CD@CdS NRs	PEC	10 fM to 1 nM	1.16	10
ERGO/PABA/AuNPs	EIS	0.1 fM to 10 nM	0.037	73
MBs−DNA−Pt NP	single-particle electrochemical collision	5 fM to 50 nM	4.86	74
graphene−nafion	EIS	100 fM to 0.1 nM	23	75
polyacrylamide gel electrophoresis assay	amperometry	100 fM to 10 nM	150	76
CdTe QDs	PEC	1 fM to 1 nM	0.65	77
hemin/G-quadruplex and (+) AuNPs	DPV	5 aM to 10 pM	1.3×10^{-3}	78
Cu-MOF@CuPc-TA-COF	PEC	1 fM to 1 nM	0.07	this work
	DPV	1 fM to 1 nM	0.18	this work

ΔI_p (nA) = 41.7 + 21.7 lg Con_{tDNA} (fM) (Figure 6b). According to the IUPAC method, the calculated LOD of 0.07 fM can be deduced within a range from 1 fM to 1 nM at the signal-to-noise ratio of 3σ, in which σ is the standard deviation of the signal in a blank solution.

Further, Figure 6c illustrates the DPV of the pDNA/Cu-MOF@CuPc-TA-COF incubated in different tDNA solutions. The peak currents of DPV curves decrease with the increase of tDNA concentration, possibly due to the increased hybridization of tDNA and pDNA, which further hampers electron transfer. Figure 6d indicates the calibration plot which displays a good linear relationship between the peak currents and the logarithm concentrations of tDNA. The linear regression equation is ΔI_E (μA) = 5.97 lg Con_{tDNA} (fM) + 5.47 (R^2 = 0.9917). As such, the LOD is calculated to be 0.18 fM according to the same method as that used for PEC. As compared with the reported HIV-1 biosensors (Table 1), the developed PEC−EC biosensor based on Cu-MOF@CuPc-TA-COF also displays the outperformed sensing performance, showing the ultralow LOD. Meanwhile, comparing the prepared PEC biosensor and the EC biosensor, the Cu-MOF@CuPc-TA-COF-based PEC biosensor displays the lower LOD and higher sensitivity.

The extremely low LOD of the developed dual-mode PEC−EC biosensor can be ascribed to the following aspects: (i) Due to the fact that the prepared Cu-MOF@CuPc-TA-COF heterostructure hybrid exhibits a large specific surface area, hierarchical structure, highly conjugated chemical component, mixed copper valence states, and rich oxygen vacancies, the synthesized hybrid shows both a superior electrochemical activity and enhanced separation ability of photogenerated carriers. These appearances hint that the synthesized hybrid can act as the superior bioplatform for PEC and EC biosensors, giving the amplified PEC or EC signals. (ii) In aqueous solution, the reserved amino groups, conjugated structure, a certain content of Cu species in the Cu-MOF@CuPc-TA-COF hybrid, and a large amount of pDNA strands can be immobilized over the hybrid due to aromatic stacking, possible metal−nitrogen interaction, and electrostatic interaction between pDNA strands and the hybrid matrix.[79] Thus, more tDNA strands can be specifically recognized using the developed biosensor, leading to the low LOD. (iii) With the porous and nanosheet structure of the Cu-MOF@CuPc-TA-COF hybrid, along with the large pores with the network, the pDNA strands with small size not only adsorb on the hybrid surface but also penetrate its interior, resulting in almost all active sites of the hybrid being able to be anchored. Consequently, no substantial nonspecific adsorption between the tDNA and matrix can occur, making the feasible construction of the dual-mode biosensor.

3.5. Selectivity, Reproducibility, Stability, and Applicability of the Dual-Mode Biosensor. The selectivity of the constructed Cu-MOF@CuPc-TA-COF-based PEC biosensor was investigated by detecting different interferents including MM2-DNA, nc-DNA, Ca^{2+}, Na^+, K^+, urea, uric acid, AFP, CEA, and MUC1 under the same determination conditions. The corresponding ΔI_p values are, respectively, 1.5 and 2 nA for analyzing MM2-DNA and nc-DNA using the biosensor, remarkably lower than that of the detection of tDNA (Figure 7a). Meantime, the other interferents also show an acceptable

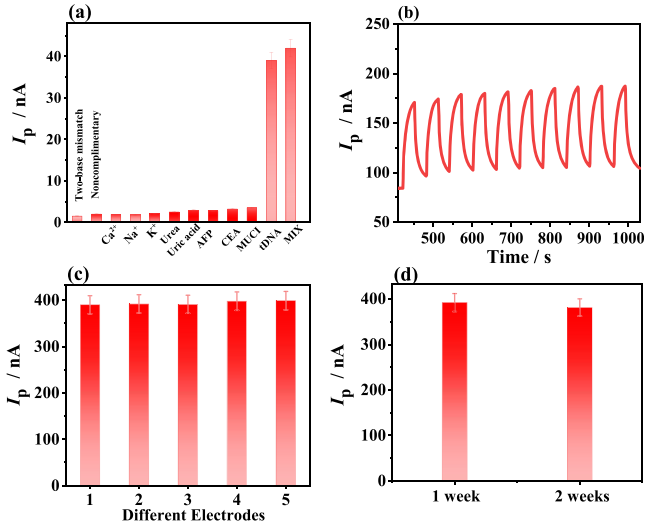

Figure 7. (a) Selectivity, (b) stability, (c) reproducibility, and (d) long-term stability of the PEC biosensor which was performed in 0.1 M PBS (pH = 7.4) (n = 3).

signal response. Hence, it is clear that the change in the PEC signal for detecting the interferents is negligible compared to that of the sensor system after the addition of tDNA, hinting at the excellent selectivity of the developed biosensor. Meanwhile, the stability of the PEC biosensor has been investigated by testing the light irradiation cycles. As shown in Figure 7b, the high stable photocurrents can be observed, indicating a good stability of response for obtaining signals. Furthermore, the reproducibility of the developed PEC biosensor was evaluated according to the intra-assay and interassay relative standard deviations (RSDs). By detecting five working electrodes, which were developed under the same experimental conditions, 1 fM tDNA was detected and showed a low RSD

https://doi.org/10.1021/acs.langmuir.1c02253
Langmuir 2021, 37, 13479−13492

value of 1.06% (Figure 7c). This suggests that the developed Cu-MOF@CuPc-TA-COF-based PEC exhibits a favorable reproducibility and precision. Apart from these, the storage stability of the developed PEC biosensor was also investigated (Figure 7d). After the pDNA/Cu-MOF@CuPc-TA-COF/GCE was stored at 4 °C for 2 weeks, the photocurrent intensity was 97.2% of the initial response when determining 1 fM tDNA, revealing the good stability of the gained biosensor.

Similarly, the selectivity of the developed DPV biosensor was also tested. Figure S15a suggests that the peak current densities of the developed biosensor for analyzing the interferents of MM2-DNA and nc-DNA are as low as 0.29 and 0.31 μA, respectively. Meanwhile, the other interferents also show a low current response in the absence of tDNA. In contrast, the obtained peak current of the detection of tDNA is remarkable. Thereby, the fabricated DPV biosensor also exhibits the outstanding selectivity for detecting tDNA. These findings hint that the developed dual-mode PEC and EC tDNA biosensor has an excellent selectivity.

Moreover, Figure S15b shows the repeated measurements of the detection of tDNA using the same five DPV biosensors, for which a low RSD of 0.6% is obtained. This indicates that the EC biosensor has good reproducibility. Also, the long-term stability of tDNA/pDNA/Cu-MOF@CuPc-TA-COF/GCE was investigated by measuring the peak current density continuously for 15 days, giving an unsubstantial change of ΔI_E with a small RSD of 1.6%. Thereby, the developed EC biosensor also displays excellent stability (Figure S15c). Subsequently, the used HIV-1 DNA biosensor was regenerated by immersing in 50 mM NaOH solution for 2 min. Afterward, it was rinsed thoroughly with PBS and dried with N_2. The renewed biosensor was then employed for the detection of tDNA again. As such, the procedure of regeneration−rinsing−detection of tDNA was repeated 15 times, for which the peak current density was recorded by the DPV technique. Figure S15d indicates that a repeatable ΔI_E can be obtained during the tDNA detection, suggesting that the proposed EC biosensor demonstrates excellent regenerability. Collectively, both the PEC and EC biosensor based on the Cu-MOF@CuPc-TA-COF hybrid possess outstanding sensing performances, such as ultralow LODs, high selectivity, good reproducibility, and remarkable stability, thus having vast practical potential applications.

3.6. Real Samples. The tDNA strands with different concentrations (1 fM, 10 fM, 100 fM, 1 pM, 10 pM, 100 pM, and 1 nM) were spiked into the pretreated human serum to evaluate the practicality of the developed biosensor. The PEC and EC biosensors were used to determine tDNA from the human serum three times. The obtained ΔI values obtained for testing different samples by PEC and DPV techniques were analyzed according to the fitting curves in Figure 6b and d, from which the tDNA concentrations were calculated and are summarized in Tables S2 and S3. Table S2 shows that the detection results obtained using the constructed PEC biosensor demonstrate acceptable recoveries from 90.2% and 109.6% and low RSDs from 0.2% and 1.9%, which are in agreement with the result obtained from RT-qPCR analysis, revealing the good reliability of the constructed PEC biosensor. As for the EC biosensor, Table S3 gives the test results of the recoveries from 90.4% to 114.8% and RSDs from 0.2% to 2.3%. Consequently, these results reveal that the developed dual-mode PEC and EC biosensor illustrates a good practicality in real samples.

4. CONCLUSION

In summary, a novel dual-mode PEC−EC was proposed for the sensitive and selective detection of the tDNA using the heterostructured MOF@COF hybrid as both the photoanode and electrode material. As compared with the pristine Cu-MOF and CuPc-TA-COF, the synthesized Cu-MOF@CuPc-TA-COF hybrid not only inherited the structural and property features of their parents, such as a highly conjugated structure, rich oxygen vacancies, mixed copper valence states (Cu^+/Cu^0), and large specific surface area, but also demonstrated the enhanced separation ability of photogenerated carriers and decreased the energy needed for semiconductor transition. Consequently, these merits of the Cu-MOF@CuPc-TA-COF hybrid afforded an excellent electrochemical activity and boosted the initial photocurrent signal. Thereby, when the Cu-MOF@CuPc-TA-COF hybrid acted as the sensing platform for immobilizing pDNA, which was the probe of tDNA, the ultralow LODs for the proposed dual-mode biosensor are obtained, 0.07 and 0.18 fM for PEC and DPV techniques, respectively, within a wide linear range of tDNA from 1 fM to 1 nM. Additionally, the developed dual-mode PEC−EC HIV-1 DNA biosensor also exhibited a high selectivity, good reproducibility, and superior stability, as well as acceptable availability. The successful application of this dual-mode PEC−EC-sensing strategy will pave a promising approach for the highly sensitive detection of other biomarkers in complex biomedical applications.

■ ASSOCIATED CONTENT

Supporting Information

The Supporting Information is available free of charge at https://pubs.acs.org/doi/10.1021/acs.langmuir.1c02253.

Reagents and materials; Cu-MOF; CuTNPc; CuTAPc; preparation of all solutions; pretreatment of the GCE; photoelectrochemical measurements and DPV; surface morphologies and nanostructures of Cu-MOF and CuPc-TA-COF; XPS spectra of Cu-MOF, CuPc-TA-COF, Cu-MOF@CuPc-TA-COF, and pDNA/Cu-MOF@CuPc-TA-COF; BET specific surface area and pore diameter of Cu-MOF, CuPC-TA-COF, and Cu-MOF@CuPc-TA-COF; SEM image and XRD spectra of tDNA/pDNA/Cu-MOF@CuPc-TA-COF; PEC and DPV curves of Cu-MOF and the CuPc-TA-COF-based biosensor; CV and EIS of the Cu-MOF@CuPc-TA-COF-based biosensor; optimization of determination conditions of the PEC biosensors; selectivity, reproducibility, stability, and regenerability of the DPV biosensor; and real sample analysis (PDF)

■ AUTHOR INFORMATION

Corresponding Authors

Zhihong Zhang − *College of Material and Chemical Engineering, Zhengzhou University of Light Industry, Zhengzhou 450001, P. R. China;* orcid.org/0000-0002-5888-4107; Email: mainzhh@163.com

Miao Du − *College of Material and Chemical Engineering, Zhengzhou University of Light Industry, Zhengzhou 450001, P. R. China;* Email: dumiao@zzuli.edu.cn

https://doi.org/10.1021/acs.langmuir.1c02253
Langmuir 2021, 37, 13479−13492

Authors

Miaoran Xu − *College of Material and Chemical Engineering, Zhengzhou University of Light Industry, Zhengzhou 450001, P. R. China*

Kun Chen − *College of Material and Chemical Engineering, Zhengzhou University of Light Industry, Zhengzhou 450001, P. R. China*

Lei Zhu − *College of Material and Chemical Engineering, Zhengzhou University of Light Industry, Zhengzhou 450001, P. R. China*

Shuai Zhang − *College of Material and Chemical Engineering, Zhengzhou University of Light Industry, Zhengzhou 450001, P. R. China*

Minghua Wang − *College of Material and Chemical Engineering, Zhengzhou University of Light Industry, Zhengzhou 450001, P. R. China*

Linghao He − *College of Material and Chemical Engineering, Zhengzhou University of Light Industry, Zhengzhou 450001, P. R. China*

Complete contact information is available at: https://pubs.acs.org/10.1021/acs.langmuir.1c02253

Notes

The authors declare no competing financial interest.

■ ACKNOWLEDGMENTS

This work was supported by the Distinguished Youth Science Foundation of Henan Province, China (202300410492) and the Key Research Project of University of Henan Province, China (19zx004).

■ REFERENCES

(1) Ethics Committee of the American Society for Reproductive Medicine. Human immunodeficiency virus (HIV) and infertility treatment: a committee opinion. *Fertil. Steril.* **2015**, *104* (1), e1−e8.

(2) Shamsipur, M.; Samandari, L.; Taherpour, A. A.; Pashabadi, A. Sub-femtomolar detection of HIV-1 gene using DNA immobilized on composite platform reinforced by a conductive polymer sandwiched between two nanostructured layers: A solid signal-amplification strategy. *Anal. Chim. Acta* **2019**, *1055*, 7−16.

(3) Zou, L.; Ling, L. Ultrasensitive detection of HIV DNA with polymerase chain reaction-dynamic light scattering. *Anal. Chem.* **2018**, *90* (22), 13373−13377.

(4) Zhang, K.; Yang, Q.; Huang, W.; Wang, K.; Zhu, X.; Xie, M. Detection of HIV-1 ribonuclease H activity in single-cell by using RNA mimics green fluorescent protein based biosensor. *Sens. Actuators B* **2019**, *281*, 439−444.

(5) Wu, Z.; Luo, F.; Wen, W.; Zhang, X.; Wang, S. Enrichment-stowage-cycle strategy for ultrasensitive electrochemiluminescent detection of HIV-DNA with wide dynamic range. *Anal. Chem.* **2019**, *91* (19), 12238−12245.

(6) Farzin, L.; Shamsipur, M.; Samandari, L.; Sheibani, S. HIV biosensors for early diagnosis of infection: The intertwine of nanotechnology with sensing strategies. *Talanta* **2020**, *206*, 120201.

(7) Liu, L.; Wang, W.; Long, J.; Fu, S.; Liang, Y.; Fu, J. Three-dimensional plasmonic photoanode of Au nanoparticles/$ZnFe_2O_4$ nanosheets coated onto ZnO nanotube arrays for photoelectrochemical production of hydrogen. *Sol. Energy Mater. Sol. Cells* **2019**, *195*, 330−338.

(8) Fu, Y.; Zou, K.; Liu, M.; Zhang, X.; Du, C.; Chen, J. Highly selective and sensitive photoelectrochemical sensing platform for VEGF165 assay based on the switching of photocurrent polarity of CdS QDs by porous Cu_2O-CuO flower. *Anal. Chem.* **2020**, *92* (1), 1189−1196.

(9) Jiang, D.; Du, X.; Liu, Q.; Hao, N.; Wang, K. MoS_2/nitrogen doped graphene hydrogels p-n heterojunction: Efficient charge transfer property for highly sensitive and selective photoelectrochemical analysis of chloramphenicol. *Biosens. Bioelectron.* **2019**, *126*, 463−469.

(10) Fan, J.; Zang, Y.; Jiang, J.; Lei, J.; Xue, H. Beta-cyclodextrin-functionalized CdS nanorods as building modules for ultrasensitive photoelectrochemical bioassay of HIV DNA. *Biosens. Bioelectron.* **2019**, *142*, 111557.

(11) Zhao, W.; Xiong, M.; Li, X.; Xu, J.; Chen, H. Photoelectrochemical bioanalysis: A mini review. *Electrochem. Commun.* **2014**, *38*, 40−43.

(12) Shu, J.; Tang, D. Recent advances in photoelectrochemical sensing: From engineered photoactive materials to sensing devices and detection modes. *Anal. Chem.* **2020**, *92* (1), 363−377.

(13) Tu, W.; Wang, Z.; Dai, Z. Selective photoelectrochemical architectures for biosensing: Design, mechanism and responsibility. *TrAC Trends Anal. Chem.* **2018**, *105*, 470−483.

(14) Yan, K.; Karthick Kannan, P.; Doonyapisut, D.; Wu, K.; Chung, C.; Zhang, J. Advanced functional electroactive and photoactive materials for monitoring the environmental pollutants. *Adv. Funct. Mater.* **2021**, *31*, 2008227.

(15) Lian, Z.; Sakamoto, M.; Matsunaga, H.; Vequizo, J. J. M.; Yamakata, A.; Haruta, M.; Kurata, H.; Ota, W.; Sato, T.; Teranishi, T. Near infrared light induced plasmonic hot hole transfer at a nano-heterointerface. *Nat. Commun.* **2018**, *9* (1), 2314.

(16) Jiang, X.; Spencer, M. G. Electrochemical impedance biosensor with electrode pixels for precise counting of CD^{4+} cells: A microchip for quantitative diagnosis of HIV infection status of AIDS patients. *Biosens. Bioelectron.* **2010**, *25* (7), 1622−1628.

(17) Kang, D.; Parolo, C.; Sun, S.; Ogden, N. E.; Dahlquist, F. W.; Plaxco, K. W. Expanding the scope of protein-detecting electrochemical DNA "scaffold" sensors. *ACS Sensors* **2018**, *3* (7), 1271−1275.

(18) Wang, J.; Hui, N. Electrochemical functionalization of polypyrrole nanowires for the development of ultrasensitive biosensors for detecting microRNA. *Sens. Actuators B* **2019**, *281*, 478−485.

(19) Xu, H.; Shang, H.; Liu, Q.; Wang, C.; Di, J.; Chen, C.; Jin, L.; Du, Y. Dual mode electrochemical-photoelectrochemical sensing platform for hydrogen sulfide detection based on the inhibition effect of titanium dioxide/bismuth tungstate/silver heterojunction. *J. Colloid Interface Sci.* **2021**, *581*, 323−333.

(20) Shang, H.; Xu, H.; Jin, L.; Wang, C.; Chen, C.; Song, T.; Du, Y. 3D $ZnIn_2S_4$ nanosheets decorated ZnCdS dodecahedral cages as multifunctional signal amplification matrix combined with electroactive/photoactive materials for dual mode electrochemical-photoelectrochemical detection of bovine hemoglobin. *Biosens. Bioelectron.* **2020**, *159*, 112202.

(21) Zhang, Q.; Fu, Y.; Xiao, K.; Du, C.; Zhang, X.; Chen, J. Sensitive dual-mode biosensors for CYFRA21−1 assay based on the dual-signaling electrochemical ratiometric strategy and "On-Off-On" PEC method. *Anal. Chem.* **2021**, *93* (17), 6801−6807.

(22) Deng, H.; Chai, Y.; Yuan, R.; Yuan, Y. In situ formation of multifunctional DNA nanospheres for a sensitive and accurate dual-mode biosensor for photoelectrochemical and electrochemical assay. *Anal. Chem.* **2020**, *92* (12), 8364−8370.

(23) Yusran, Y.; Fang, Q.; Valtchev, V. Electroactive covalent organic frameworks: design, synthesis, and applications. *Adv. Mater.* **2020**, *32* (44), 2002038.

(24) Feng, Y.; Yan, T.; Wu, T.; Zhang, N.; Yang, Q.; Sun, M.; Yan, L.; Du, B.; Wei, Q. A label-free photoelectrochemical aptasensing platform base on plasmon Au coupling with MOF-derived In_2O_3@g-C_3N_4 nanoarchitectures for tetracycline detection. *Sens. Actuators B* **2019**, *298*, 126817.

(25) Dai, L.; Li, Y.; Wang, Y.; Luo, X.; Wei, D.; Feng, R.; Yan, T.; Ren, X.; Du, B.; Wei, Q. A prostate-specific antigen electrochemical immunosensor based on Pd NPs functionalized electroactive Co-

MOF signal amplification strategy. *Biosens. Bioelectron.* **2019**, *132*, 97−104.
(26) Liu, B.; Wang, X.; Liu, H.; Zhai, Y.; Li, L.; Wen, H. 2D MOF with electrochemical exfoliated graphene for nonenzymatic glucose sensing: Central metal sites and oxidation potentials. *Anal. Chim. Acta* **2020**, *1122*, 9−19.
(27) Huang, J.; Liu, X.; Zhang, W.; Liu, Z.; Zhong, H.; Shao, B.; Liang, Q.; Liu, Y.; Zhang, W.; He, Q. Functionalization of covalent organic frameworks by metal modification: Construction, properties and applications. *Chem. Eng. J.* **2021**, *404*, 127136.
(28) Lv, M.; Zhou, W.; Tavakoli, H.; Bautista, C.; Xia, J.; Wang, Z.; Li, X. Aptamer-functionalized metal-organic frameworks (MOFs) for biosensing. *Biosens. Bioelectron.* **2021**, *176*, 112947.
(29) Ren, X.; Liao, G.; Li, Z.; Qiao, H.; Zhang, Y.; Yu, X.; Wang, B.; Tan, H.; Shi, L.; Qi, X.; Zhang, H. Two-dimensional MOF and COF nanosheets for next-generation optoelectronic applications. *Coord. Chem. Rev.* **2021**, *435*, 213781.
(30) Wang, M.; Pan, Y.; Wu, S.; Sun, Z.; Wang, L.; Yang, J.; Yin, Y.; Li, G. Detection of colorectal cancer-derived exosomes based on covalent organic frameworks. *Biosens. Bioelectron.* **2020**, *169*, 112638.
(31) Lu, K.; Aung, T.; Guo, N.; Weichselbaum, R.; Lin, W. Nanoscale metal-organic frameworks for therapeutic, imaging, and sensing applications. *Adv. Mater.* **2018**, *30* (37), 1707634.
(32) Ma, X.; Ding, W.; Wang, C.; Wu, H.; Tian, X.; Lyu, M.; Wang, S. DNAzyme biosensors for the detection of pathogenic bacteria. *Sens. Actuators B* **2021**, *331*, 129422.
(33) Kong, W.; Guo, X.; Jing, M.; Qu, F.; Lu, L. Highly sensitive photoelectrochemical detection of bleomycin based on Au/WS_2 nanorod array as signal matrix and Ag/ZnMOF nanozyme as multifunctional amplifier. *Biosens. Bioelectron.* **2020**, *150*, 111875.
(34) Liu, X.; Zhao, Y.; Li, F. Nucleic acid-functionalized metal-organic framework for ultrasensitive immobilization-free photoelectrochemical biosensing. *Biosens. Bioelectron.* **2021**, *173*, 112832.
(35) Zhang, G.; Zhuang, Y.; Shan, D.; Su, G.; Cosnier, S.; Zhang, X. Zirconium-based porphyrinic metal-organic framework (PCN-222): Enhanced photoelectrochemical response and its application for label-free phosphoprotein detection. *Anal. Chem.* **2016**, *88* (22), 11207−11212.
(36) Zang, Y.; Fan, J.; Ju, Y.; Xue, H.; Pang, H. Current advances in semiconductor nanomaterial-based photoelectrochemical biosensing. *Chem. Eur. J.* **2018**, *24* (53), 14010−14027.
(37) Yan, T.; Wu, T.; Wei, S.; Wang, H.; Sun, M.; Yan, L.; Wei, Q.; Ju, H. Photoelectrochemical competitive immunosensor for 17β-estradiol detection based on $ZnIn_2S_4$@NH_2-MIL-125(Ti) amplified by PDA NS/Mn: ZnCdS. *Biosens. Bioelectron.* **2020**, *148*, 111739.
(38) Wei, Q.; Wang, C.; Zhou, X.; Wu, T.; Wang, Y.; Li, C.; Yang, N. Ionic liquid and spatially confined gold nanoparticles enhanced photoelectrochemical response of zinc-metal organic frameworks and immunosensing squamous cell carcinoma antigen. *Biosens. Bioelectron.* **2019**, *142*, 111540.
(39) Zhang, L.; Feng, L.; Li, P.; Chen, X.; Jiang, J.; Zhang, S.; Zhang, C.; Zhang, A.; Chen, G.; Wang, H. Direct Z-scheme photocatalyst of hollow CoSx@CdS polyhedron constructed by ZIF-67-templated one-pot solvothermal route: A signal-on photoelectrochemical sensor for mercury (II). *Chem. Eng. J.* **2020**, *395*, 125072.
(40) Yang, R.; Yan, X.; Li, Y.; Zhang, X.; Chen, J. Nitrogen-doped porous carbon-ZnO nanopolyhedra derived from ZIF-8: New materials for photoelectrochemical biosensors. *ACS Appl. Mater. Interfaces* **2017**, *9* (49), 42482−42491.
(41) Zhang, X.; Chi, K.; Li, D.; Deng, Y.; Ma, Y.; Xu, Q.; Hu, R.; Yang, Y. 2D-porphrinic covalent organic framework-based aptasensor with enhanced photoelectrochemical response for the detection of C-reactive protein. *Biosens. Bioelectron.* **2019**, *129*, 64−71.
(42) Zhang, X.; Li, G.; Wu, D.; Zhang, B.; Hu, N.; Wang, H.; Liu, J.; Wu, Y. Recent advances in the construction of functionalized covalent organic frameworks and their applications to sensing. *Biosens. Bioelectron.* **2019**, *145*, 111699.
(43) Li, H.; Sui, Z. An in situ coupling strategy for the preparation of heterometal-doped carbon frameworks as efficient bifunctional ORR/OER electrocatalysts. *New J. Chem.* **2019**, *43* (46), 17963−17973.
(44) Singh, A.; Roy, S.; Das, C.; Samanta, D.; Maji, T. K. Metallophthalocyanine-based redox active metal-organic conjugated microporous polymers for OER catalysis. *Chem. Commun.* **2018**, *54* (35), 4465−4468.
(45) Zhang, H.; Gu, C.; Yao, M.; Kitagawa, S. Hybridization of emerging crystalline porous materials: Synthesis dimensionality and electrochemical energy storage application. *Adv. Energy Mater.* **2021**, 2100321.
(46) Zhang, L.; Liu, Z.; Deng, Q.; Sang, Y.; Dong, K.; Ren, J.; Qu, X. Nature-inspired construction of MOF@COF nanozyme with active sites in tailored microenvironment and pseudopodia-like surface for enhanced bacterial inhibition. *Angew. Chem. Int. Ed.* **2021**, *60* (7), 3469−3474.
(47) Peng, H.; Raya, J.; Richard, F.; Baaziz, W.; Ersen, O.; Ciesielski, A.; Samorì, P. Synthesis of robust MOFs@COFs porous hybrid materials via an Aza-Diels-Alder Reaction: Towards high-performance supercapacitor materials. *Angew. Chem. Int. Ed.* **2020**, *59* (44), 19602−19609.
(48) Gao, M.; Qi, M.; Liu, L.; Han, Z. An exceptionally stable core-shell MOF/COF bifunctional catalyst for a highly efficient cascade deacetalization-Knoevenagel condensation reaction. *Chem. Commun.* **2019**, *55* (45), 6377−6380.
(49) Li, F.; Wang, D.; Xing, Q.; Zhou, G.; Liu, S.; Li, Y.; Zheng, L.; Ye, P.; Zou, J. Design and syntheses of MOF/COF hybrid materials via postsynthetic covalent modification: An efficient strategy to boost the visible-light-driven photocatalytic performance. *Appl. Catal. B* **2019**, *243*, 621−628.
(50) Peng, Y.; Zhao, M.; Chen, B.; Zhang, Z.; Huang, Y.; Dai, F.; Lai, Z.; Cui, X.; Tan, C.; Zhang, H. Hybridization of MOFs and COFs: A new strategy for construction of MOF@COF core-shell hybrid materials. *Adv. Mater.* **2018**, *30* (3), 1705454.
(51) Zhang, F.; Sheng, J.; Yang, Z.; Sun, X.; Tang, H.; Lu, M.; Dong, H.; Shen, F.; Liu, J.; Lan, Y. Rational design of MOF/COF hybrid materials for photocatalytic H_2 evolution in the presence of sacrificial electron donors. *Angew. Chem. Int. Ed.* **2018**, *57* (37), 12106−12110.
(52) Garzón-Tovar, L.; Pérez-Carvajal, J.; Yazdi, A.; Hernández-Muñoz, J.; Tarazona, P.; Imaz, I.; Zamora, F.; Maspoch, D. A MOF@COF composite with enhanced uptake through interfacial pore generation. *Angew. Chem. Int. Ed.* **2019**, *58* (28), 9512−9516.
(53) Li, Y.; Karimi, M.; Gong, Y.; Dai, N.; Safarifard, V.; Jiang, H. Integration of metal-organic frameworks and covalent organic frameworks: Design, synthesis, and applications. *Matter* **2021**, *4* (7), 2230−2265.
(54) Zhou, N.; Ma, Y.; Hu, B.; He, L.; Wang, S.; Zhang, Z.; Lu, S. Construction of Ce-MOF@COF hybrid nanostructure: Label-free aptasensor for the ultrasensitive detection of oxytetracycline residues in aqueous solution environments. *Biosens. Bioelectron.* **2019**, *127*, 92−100.
(55) Wang, X.; Yin, H.; Yin, X. MOF@COFs with strong multi-emission for differentiation and ratiometric fluorescence detection. *ACS Appl. Mater. Interfaces* **2020**, *12* (18), 20973−20981.
(56) Jampasa, S.; Pummoree, J.; Siangproh, W.; Khongchareonporn, N.; Ngamrojanavanich, N.; Chailapakul, O.; Chaiyo, S. Signal-On" electrochemical biosensor based on a competitive immunoassay format for the sensitive determination of oxytetracycline. *Sens. Actuators B* **2020**, *320*, 128389.
(57) Bai, X.; Zhang, Y.; Gao, W.; Zhao, D.; Yang, D.; Jia, N. Hollow ZnS-CdS nanocage based photoelectrochemical sensor combined with molecularly imprinting technology for sensitive detection of oxytetracycline. *Biosens. Bioelectron.* **2020**, *168*, 112522.
(58) Mei, L.; Cui, X.; Duan, Q.; Li, Y.; Lv, X.; Wang, H. Metal phthalocyanine-linked conjugated microporous polymer hybridized with carbon nanotubes as a high-performance flexible electrode for supercapacitors. *Int. J. Hydrogen Energy* **2020**, *45* (43), 22950−22958.

https://doi.org/10.1021/acs.langmuir.1c02253
Langmuir 2021, 37, 13479−13492

(59) Liao, Z.; Wang, Y.; Wang, Q.; Cheng, Y.; Xiang, Z. Bimetal-phthalocyanine based covalent organic polymers for highly efficient oxygen electrode. *Appl. Catal. B* **2019**, *243*, 204−211.
(60) Allegrini, F.; Olivieri, A. C. IUPAC-Consistent Approach to the limit of detection in partial least-squares calibration. *Anal. Chem.* **2014**, *86* (15), 7858−7866.
(61) Liu, T.; Cui, L.; Zhao, H.; Zhang, X. In situ generation of regularly ordered 2D ultrathin covalent organic framework films for highly sensitive photoelectrochemical bioanalysis. *ACS Appl. Mater. Interfaces* **2020**, *12* (41), 47090−47098.
(62) Yang, Y.; Niu, H.; Xu, L.; Zhang, H.; Cai, Y. Triazine functionalized fully conjugated covalent organic framework for efficient photocatalysis. *Appl. Catal. B* **2020**, *269*, 118799.
(63) Yang, Y.; Yan, W.; Wang, X.; Yu, L.; Zhang, J.; Bai, B.; Guo, C.; Fan, S. Development of a molecularly imprinted photoelectrochemical sensing platform based on NH_2-MIL-125(Ti)-TiO_2 composite for the sensitive and selective determination of oxtetracycline. *Biosens. Bioelectron.* **2021**, *177*, 113000.
(64) Zhao, R.; Mei, L.; Wang, L.; Chai, Z. F.; Shi, W. Q. Copper/Zinc-directed heterometallic uranyl-organic polycatenating frameworks: Synthesis, characterization, and anion-dependent structural regulation. *Inorg. Chem.* **2016**, *55* (20), 10125−10134.
(65) Li, C.; He, J.; Xiao, Y.; Li, Y.; Delaunay, J. Earth-abundant Cu-based metal oxide photocathodes for photoelectrochemical water splitting. *Energy Environ. Sci.* **2020**, *13* (10), 3269−3306.
(66) Yang, Z.; Zhuo, Y.; Yuan, R.; Chai, Y. Electrochemical activity and electrocatalytic property of cobalt phthalocyanine nanoparticles-based immunosensor for sensitive detection of procalcitonin. *Sens. Actuators B* **2016**, *227*, 212−219.
(67) Jin, S.; Ma, X.; Pan, J.; Zhu, C.; Saji, S. E.; Hu, J.; Xu, X.; Sun, L.; Yin, Z. Oxygen vacancies activating surface reactivity to favor charge separation and transfer in nanoporous $BiVO_4$ photoanodes. *Appl. Catal. B* **2021**, *281*, 119477.
(68) Wang, D.; Su, B.; Jiang, Y.; Li, L.; Ng, B. K.; Wu, Z.; Liu, F. Polytype 1T/2H MoS_2 heterostructures for efficient photoelectrocatalytic hydrogen evolution. *Chem. Eng. J.* **2017**, *330*, 102−108.
(69) Hao, H.; Lu, D.; Wang, Q. Photoelectrochemical study on charge separation mechanisms of Bi_2WO_6 quantum dots decorated g-C_3N_4. *Int. J. Hydrogen Energy* **2018**, *43* (18), 8824−8834.
(70) Wang, H.; Ma, R.; Sun, F.; Jia, L.; Zhang, W.; Shang, L.; Xue, Q.; Jia, W.; Wang, H. A versatile label-free electrochemical biosensor for circulating tumor DNA based on dual enzyme assisted multiple amplification strategy. *Biosens. Bioelectron.* **2018**, *122*, 224−230.
(71) Jia, Z.; Ma, Y.; Yang, L.; Guo, C.; Zhou, N.; Wang, M.; He, L.; Zhang, Z. $NiCo_2O_4$ spinel embedded with carbon nanotubes derived from bimetallic NiCo metal-organic framework for the ultrasensitive detection of human immune deficiency virus-1 gene. *Biosens. Bioelectron.* **2019**, *133*, 55−63.
(72) Wang, S.; Zhao, J.; Zhang, Y.; Yan, M.; Zhang, L.; Ge, S.; Yu, J. Photoelectrochemical biosensor of HIV-1 based on cascaded photoactive materials and triple-helix molecular switch. *Biosens. Bioelectron.* **2019**, *139*, 111325.
(73) Cui, Y.; Li, B.; He, H.; Zhou, W.; Chen, B.; Qian, G. Metal-organic frameworks as platforms for functional materials. *Acc. Chem. Res.* **2016**, *49* (3), 483−493.
(74) Ye, T.; Liu, Y.; Luo, M.; Xiang, X.; Ji, X.; Zhou, G.; He, Z. Metal-organic framework-based molecular beacons for multiplexed DNA detection by synchronous fluorescence analysis. *Analyst* **2014**, *139* (7), 1721−1725.
(75) Chen, L.; Zheng, H.; Zhu, X.; Lin, Z.; Guo, L.; Qiu, B.; Chen, G.; Chen, Z. Metal-organic frameworks-based biosensor for sequence-specific recognition of double-stranded DNA. *Analyst* **2013**, *138* (12), 3490−3493.
(76) Zhao, H.; Qiu, G.; Liang, Z.; Li, M.; Sun, B.; Qin, L.; Yang, S.; Chen, W.; Chen, J. A zinc(II)-based two-dimensional MOF for sensitive and selective sensing of HIV-1 ds-DNA sequences. *Anal. Chim. Acta* **2016**, *922*, 55−63.
(77) Pan, Y.; Zhan, S.; Xia, F. Zeolitic imidazolate framework-based biosensor for detection of HIV-1 DNA. *Anal. Biochem.* **2018**, *546*, 5−9.
(78) Li, Z.; Xu, H.; Li, S.; Wu, S.; Miao, X. Zettomole electrochemical HIV DNA detection using 2D DNA-Au nanowire structure, hemin/G-quadruplex and polymerase chain reaction multi-signal synergistic amplification. *Anal. Chim. Acta* **2021**, *1159*, 338428.
(79) Gong, Q.; Han, H.; Yang, H.; Zhang, M.; Sun, X.; Liang, Y.; Liu, Z.; Zhang, W.; Qiao, J. Sensitive electrochemical DNA sensor for the detection of HIV based on a polyaniline/graphene nanocomposite. *J. Materiom.* **2019**, *5* (2), 313−319.

https://doi.org/10.1021/acs.langmuir.1c02253
Langmuir 2021, 37, 13479−13492